Formation of chevrons in the dielectric regime of electroconvection in nematic liquid crystals

M. Scheuring, L. Kramer, and J. Peinke
Physics Institute, University of Bayreuth, D-95440 Bayreuth, Germany
(Received 17 October 1997)

We present quantitative measurements of the scenario leading to chevrons in the dielectric range of ac driven electroconvection in a planarly aligned layer of the nematic liquid crystal Merck Phase 5. First, we demonstrate that the threshold of electroconvection is described correctly by the standard theory. Second, we characterize above threshold the appearance of chevrons out of the defect chaotic state by a rather sudden increase of the density of defects. Furthermore, we show that the spatial correlations between defects characterizing the chevrons set in simultaneously. Finally, we give the onset curve of chevrons (voltage versus frequency) and also discuss briefly their further development. [S1063-651X(98)09608-1]

PACS number(s): 61.30.−v, 64.70.−p, 47.20.−k

I. INTRODUCTION

Electroconvection (EC) in planarly aligned nematic liquids has become the prime example for anisotropic convection [1–3]. In EC, a nematic slab (thickness $d\sim 10-100\ \mu$m) is sandwiched between two conducting plates with an electric field applied across (in the z direction). The anisotropy is introduced by planar anchoring of the nematic director $\mathbf{n}$ at the bounding plates along a fixed axis (the x direction). $\mathbf{n}=(n_x,n_y,n_z)$ stands for the mean orientation of the highly anisotropic molecules ($|\mathbf{n}|=1$). Spatial and temporal patterns involving $\mathbf{n}$ and the velocity field $\mathbf{v}$ arise if a sufficiently high electric field acts on the liquid crystal. The mechanism is well understood [4–6,3]. It involves space charges created mainly as a result of the anisotropic conductivity, which leads to convection via the electrostatic body force.

Slightly above threshold of EC a pattern of periodic convection rolls appears. In contrast to the case of an isotropic system, such as Rayleigh-Bénard convection in simple fluids [7], the anisotropy allows us to obtain very homogeneous patterns of large aspect ratios (typically up to 500 rolls). Depending on the frequency f of the applied ac voltage $V(t)=\sqrt{2}V_0\sin(2\pi ft)$, one distinguishes between the low-frequency conduction regime ($f<f_d$) and the higher-frequency dielectric regime ($f>f_d$). The latter essentially exists only for materials with negative dielectric anisotropy. (This results from the competition of the stabilizing dielectric force and the destabilizing body force.) The crossover frequency $f_d\approx 20-1000$ Hz scales with $(2\pi\tau_q)^{-1}$, where $\tau_q=\epsilon_0\epsilon_\perp/\sigma_\perp$ is the charge relaxation time. (As usual, in the definition we chose the permittivity and conductivity perpendicular to the director.)

The wave number of rolls in the well-studied conduction regime is of the order of π/d. This is the typical situation found in convection instabilities. In fact, one can argue that the appearance of the periodic pattern is connected with the constraint imposed on the flow by the geometry once the destabilization mechanism has become effective [8,3]. The orientation of the rolls is either oblique ($f<f_L$) or normal ($f>f_L$) with respect to the x direction. One exemplary pattern of normal conduction rolls from our experiments is shown in Fig. 1(a).

In this work we are concerned with the dielectric regime. Some measurements of the threshold behavior in the conduction regime are included only for completeness. In the dielectric regime, the wave number of the rolls is usually much larger (wavelengths are typically in the range of several micrometers or smaller), which means that the rolls are very narrow; see Fig. 1(b) as an example. The rolls are found to be normal. The shorter wavelength in the dielectric regime is due to the fact that the applied ac field forces the director to oscillate rapidly with frequency f around the planar orientation. This introduces an (elastic) bend deformation of the director field. Such oscillations decay in the x direction with

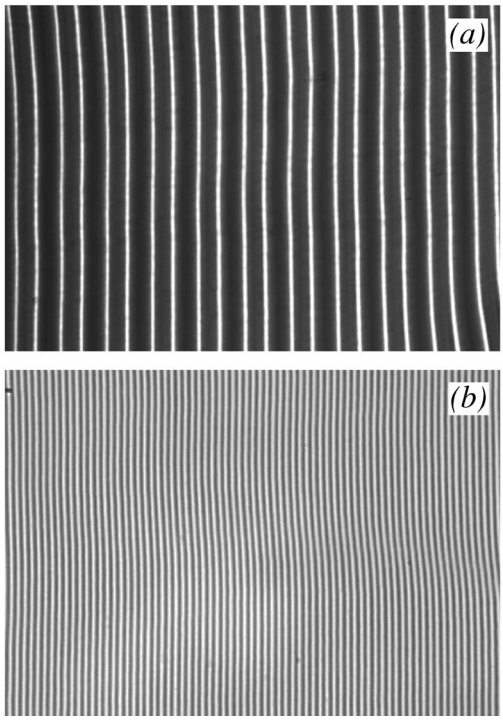

FIG. 1. Shadowgraph images of typical roll structures near the threshold. (a) Normal rolls for $f=20$ Hz (the sample thickness is 36 μm); the section shown corresponds to $832\times 582\ \mu$m^2. (b) Dielectric rolls for $f=45$ Hz (the sample thickness is 24 μm); the section shown corresponds to $307\times 235\ \mu$m^2. The alignment of the director is in the x direction.

 © 1998 The American Physical Society

the bend diffusion length $\sqrt{2\pi f K_3/|\alpha_2|}$, which sets the scale for the wavelength. Here K_3 and α_2 denote, respectively, the bend diffusion constant and the appropriate rotational viscosity. Some properties of dielectric rolls connected with the rapid time oscillations of the director have been measured [9,10].

Increasing the amplitude V_0 of the voltage beyond the threshold V_c [we use the dimensionless control parameter $\epsilon = (V^2 - V_c^2)/V_c^2$], one finds in the dielectric range very quickly a destabilization of rolls by the appearance of defects. These defects correspond to dislocations in the periodic pattern, where a roll pair starts or ends corresponding to a topological charge ± 1. This brings the system into a state of persistent complex dynamics (defect chaos). The density of defects increases with ϵ. At a point still rather near threshold, the defects start to develop spatial correlations, which lead to a state with a (partial) ordering of defects along a periodic array of chains. The chains have the following characteristic features: First, they are oriented along the y direction, i.e., parallel to the undisturbed rolls; second, each chain consists of defects of the same topological charge; third, the charge alters from chain to chain. The rolls in the regions between chains are alternatively rotated to the left and to the right (for simple topological reasons), which gives this structure its characteristic herringbonelike appearance called chevrons. Although chevrons have been known for more than 25 years [11] (pictures can be found in the standard texts on liquid crystals [12]), the scenario leading to chevrons, as well as the properties of the chevron state, have not been studied quantitatively. Our work is intended to fill this gap. Hopefully it may be useful to test models for chevron formation, such as the one suggested very recently [13].

II. EXPERIMENTAL SETUP

The experimental setup is the standard capacitor-type cell [1,2] with the nematic liquid crystal sandwiched between two parallel transparent electrodes. As nematic we used Merck Phase 5, a eutectic mixture of azoxy compounds. The surfaces of the transparent electrodes were coated with polymer and rubbed in one direction to produce homogeneous, planar alignments of the director. The typical dimension of the electrodes was in the range of centimeters, whereas the thickness d of the nematic layer, controlled by Mylar spacers between the electrodes, was (nominally) between 10 and 40 μm. Here we report on measurements on three samples with nominal thicknesses of 14.8, 24, and 36.4 μm. A custom-built sampleholder together with a thermostat (Lauda RM6) guaranteed a temperature stability of better than 0.1 °C. All experiments were done at $T = 20$ °C. Voltage amplitudes $0 < V_0 < 120$ V and frequencies 1 Hz $< f <$ 1 kHz were used. The patterns in the liquid crystal were visualized by the shadowgraph method [14]. With a microscope (Leitz Laborlux 12 Pol S) and a charge coupled device camera we could either display the patterns on a TV screen, record them on a video recorder, or save single images via a frame grabber on a personal computer (PC).

The whole experimental system could be controlled by a PC. Usually experimental runs lasting several hours were controlled by the PC and the patterns of the liquid crystal were recorded on a videotape. Subsequently single images were digitized, with a spatial resolution of 512×512 and an eight-bit gray scale. These images were analyzed further.

III. THRESHOLD OF CONVECTION

We first measured the threshold behavior for the appearance of rolls. A comparison with theory showed that the system behaved according to the conventional theory; cf. [3]. In order to obtain an accuracy of better than 1% for $V_c(f)$ we applied the following procedure. As a starting point for each measurement at a given frequency, an undercritical voltage V_0 was selected (no pattern visible). V_0 was increased in steps varying between 20 mV (conduction regime) and 40 mV (dielectric regime). After each change of the parameters, we waited for a time longer than the relevant relaxation time ($\approx 1-10$ s) to let the system relax into a steady state. Then several shadowgraph images were recorded. In the conduction regime we focused on the $E3$ plane, whereas in the dielectric regime the $E1$ focal plane was used for the shadowgraph imaging; see [14]. With the change of frequency, the focus had to be corrected from time to time. For each image the contrast K was determined by the formula

$$K = \langle K_j \rangle = \left\langle \sqrt{\frac{1}{512} \sum_{i=1}^{512} \frac{(b_{ij} - z_{ij} - \langle b_j - z_j \rangle)^2}{\langle z_j \rangle^2}} \right\rangle, \quad (1)$$

where b_{ij} is the intensity of the ith pixel in the jth line and z_{ij} is the intensity of the corresponding pixel of an image without pattern taken at $V_0 < V_c$ (background). b_j and z_j denote the mean values of the corresponding intensities taken over one line; angular brackets denote the average over different lines. Usually, 100 different lines of one picture were used to determine the contrast K.

As shown in Figs. 2(a) and 2(b), the threshold V_c as well as the slope $S = dK/dV$ can be estimated quite accurately in the conduction and in the dielectric regime by a simple linear fit. The slope S plotted in Fig. 2(c) vs frequency will be discussed later. For the three samples with thicknesses 14.8, 24, and 36.4 μm, the threshold curves $V_c(f)$ together with the wave number $q_c(f)$ at threshold was determined systematically as a function of the frequency by the abovementioned method. We only show results for $d = 24$ μm; see Figs. 3 and 4 (solid circles). The wave numbers were obtained from the Fourier transform of x-line scans of several different images.

In Fig. 3 one sees a clear break in the monotonic increase of V_c with the frequency at f_d, which signifies the separation between the conduction and the dielectric regime. Within some weeks after sample preparation, the crossover frequency f_d increased to some extent. Only fresh samples were used in the measurements. In the conduction regime V_c follows rather closely a quadratic law, whereas in the dielectric regime V_c is found to scale approximately with the square root of the frequency. Of course the jump in q_c at f_d is even more dramatic ($q_c \sim f^{1/2}$ in the dielectric regime). The measurements on the other samples confirm the general understanding that V_c in the conduction regime is rather independent of the thickness, whereas in the dielectric regime it is approximately proportional to d. For the wave number q_c we

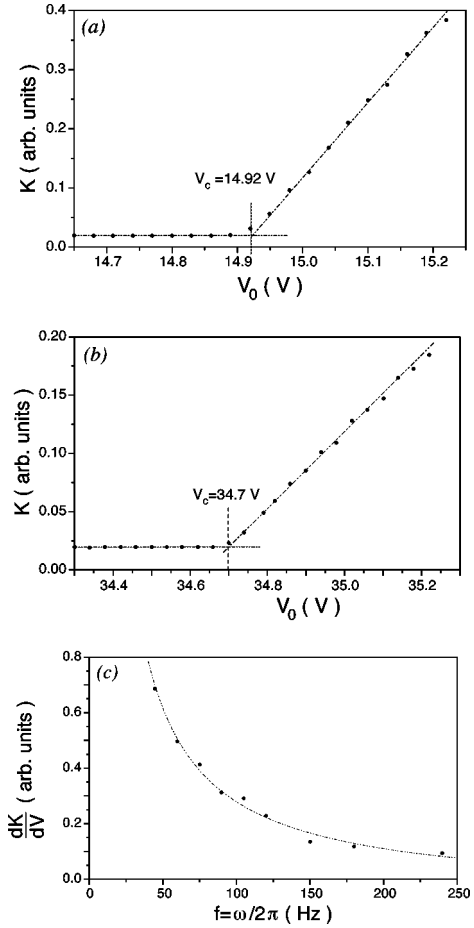

FIG. 2. Contrast as a function of the applied voltage amplitude V_0 for (a) the conduction regime with normal rolls, $f=20$ Hz, and (b) the dielectric regime, $f=90$ Hz. (c) Slope of the contrast at the threshold voltage V_c as a function of the frequency f. The dashed curve represents a fit by S_0/f, where S_0 denotes a constant.

find the inverse behavior, namely, q_c is independent of d in the dielectric regime and dependent on d in the conduction regime.

Next, a comparison of our measurements with results from the standard theory of electroconvection was done. To

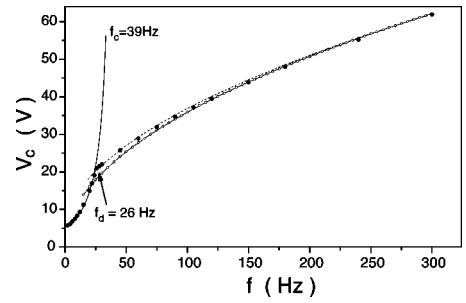

FIG. 3. Critical voltage V_c as a function of the frequency. f_d denotes the transition frequency separating the conduction regime ($f<f_d$) and the dielectric regime ($f>f_d$). Roll patterns always form for parameter values above the measured data points. The different curves correspond to theoretical predictions. In the dielectric range the lower solid line corresponds to an analytic approximation [3,17], whereas the upper dotted line represents the numerical treatment [16]. In the conduction range only the numerical results from [16] are shown. The sample thickness $d=24$ μm.

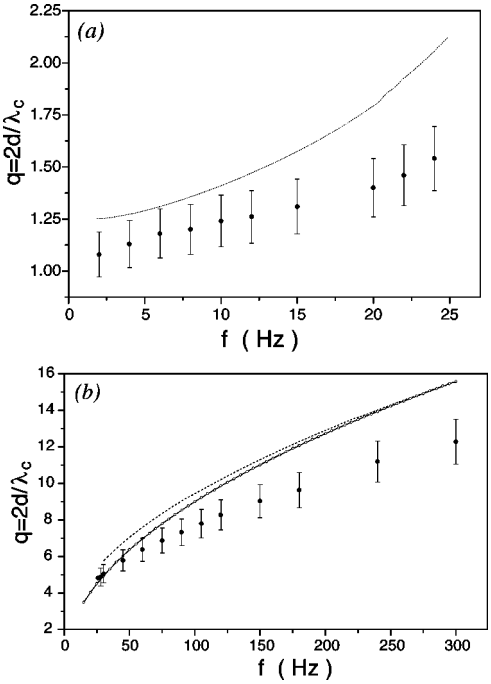

FIG. 4. Dimensionless wave number at the threshold in (a) the conduction and (b) the dielectric regime. For further details see Fig. 3.

determine the threshold curves $V_c(f)$ and $q_c(f)$ one starts from the basic electrohydrodynamic equations of nematic fluids. They involve momentum balance (Navier-Stokes equation), the rate equation for the director, as well as charge conservation together with Ohm's law and the Poisson equation. Due to the anisotropy of the material, the equations are rather complicated and contain in particular five viscosities. The flexoelectric effect is neglected. The equations are linearized around the basic state where the velocities are zero, the director is everywhere oriented along x, and electric current flows with the conductivity $\sigma_\perp$ in the z direction.

The equations are to be supplemented by boundary conditions. Periodicity is demanded in the x-y plane, which leads to harmonic behavior. Since we may specialize to normal rolls the modal solutions are characterized by the wave number q. Their time behavior is essentially exponential with a growth rate that turns out to be real in the relevant range. Since one has ac excitation with frequency f, the system is driven parametrically in time (the time exponent is really a Floquet-Bloch exponent) and there remains a periodic time dependence, which is treated by a (truncated) Fourier expansion with fundamental frequency f. The conduction and dielectric modes differ in their time symmetry. In the conduction mode, the electric quantities (e.g., the charge density) have odd Fourier components, whereas the velocity and the director have even ones. Here we used truncation at lowest meaningful order, which is usually a reasonable approximation. There remains the problem of the z dependence, which in this case is treated by an approximation with test functions satisfying appropriate boundary conditions and having the correct symmetry (''one-mode approximation''). From the condition that the growth rate becomes positive for the first time, the threshold and the critical wave number q_c as well as the type of mode (conduction or dielectric) are

obtained. Although much of this procedure can be developed analytically, a numerical evaluation is needed ultimately; see [3,15,16]. For the dielectric mode, variations in the z direction are slow compared to those in the x direction. A meaningful analytic approximation is obtained by neglecting all z dependence [3,17]. This approximation has been included in Figs. 3 and 4 (dotted) in addition to the numerical results (solid).

The conduction regime has been used to fit the material parameters $k_{33}, \sigma_{\perp}$, and $\sigma_{||}$, but no attempt was made to obtain an optimal fit for the dielectric range and for the wave-number behavior. The ratios k_{11}/k_{33} and k_{22}/k_{33} were taken from the standard material N-(4-methoxybenzylidene-4-butylaniline (MBBA). Meanwhile, measurements of the elastic constants of Phase 5 at $T=30\,^{\circ}\mathrm{C}$ have become available [18]. In Ref. [18] also a thorough comparison between the experimental threshold behavior and theory is presented for the conduction regime. The parameters used here are listed in [19]. From Fig. 3 we conclude that our measurements of V_c are described quite accurately by the theory. The systematic discrepancy in the critical wave number q_c (see Fig. 4) could indicate that the actual thickness d is somewhat larger than that of the spacers, which is not unusual. Nevertheless, we want to point out that the functional behavior of the experimental data of q_c is in good accordance with the theory.

Next we want to discuss some implications of the measurements of the contrast V_c and q_c. Whereas in the conduction regime a comparison between experiment and theory has been done for these quantities [15], we report here on corresponding results for the dielectric range. Above V_c, the observed linear rise of the contrast indicates that $K-K_0 \approx \theta_0^2 F(q)$, with $\theta_0^2 \approx \epsilon/g(q)$. Here θ_0 denotes the amplitude of the out-of-plane angle of the director of the nematic, which can be taken as the proper order parameter. F and the Landau coefficient g denote functions of the wave vector q. An analysis of the shadowgraph optics shows that the relation for K should hold for the focal planes selected [14]. The usual assumption is $F(q) \propto q^2$. The second relation for θ_0^2 (with the Landau coefficient $g>0$) signifies a supercritical pitchfork bifurcation, which is expected in the conduction as well as in the dielectric range (see, e.g., [2]), at least on the level of the sensitivity of our experiments [20]. From the slope $S=dK/dV \approx (K-K_0)/\epsilon V_c$ in Fig. 2 it is in principle possible to determine g $[g \approx \epsilon/\theta_0^2 \approx \epsilon F(q_c)/(K-K_0) \approx F(q_c)/V_c S]$ if $F(q_c)$ is known.

As shown in Fig. 2(c), in the dielectric range a decrease of S with increasing frequency is found. This decrease can be described by $S \approx S_0/f$ in the range $50<f<250$ Hz. From a recent theoretical prediction that g should be independent of frequency [21], together with $V_c \sim f^{1/2}$, one deduces $F(q_c) \sim f^{-1/2}$, which is incompatible with $F(q) \sim q^2$ since q_c definitely increases with f. Presumably the discrepancy is explained by the fact that in these measurements one is approaching the limit of resolution of the camera and the microscope, where the relation $F(q) \propto q^2$ breaks down.

IV. CHEVRONS

In this section we present for the dielectric regime a detailed study of the scenario leading to chevrons. This scenario occurs above threshold in a fairly narrow range of ϵ, at least for not too thin and too clean cells. In Fig. 5 the sequence of patterns observed for increasing ϵ is shown. First, a state with a low density of irregularly moving defects emerges. Each defect can be characterized by the topological charge T,

$$T = \frac{1}{2\pi} \oint \nabla \phi \cdot d\mathbf{s} = \pm 1, \tag{2}$$

where the integral is to be taken around the defect in the positive sense. For the periodic pattern, i.e., in the absence of any defects, the phase is given by $\phi = qx + \phi_0$. The defect modulates the phase and it is not defined at the center of the defect (see below). For topological reasons, and as observed

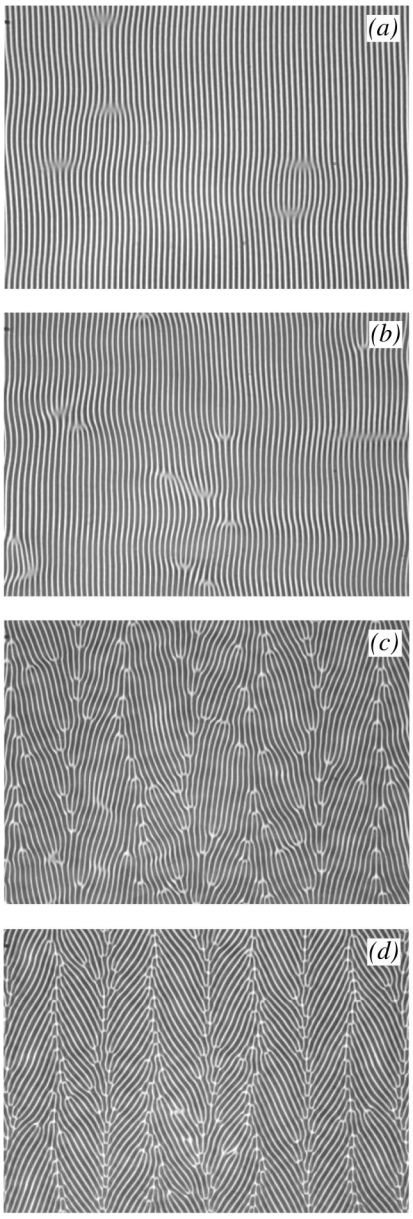

FIG. 5. Sequence of snapshots demonstrating the route from dielectric rolls to chevrons for the sample with $d=24$ μm and $f=45$ Hz. (a) Well-separated defects for $\epsilon=0.08$, (b) higher density of defects for $\epsilon=0.165$, (c) defects organized in chevrons for $\epsilon=0.24$, and (d) well-developed chevrons for $\epsilon=0.35$.

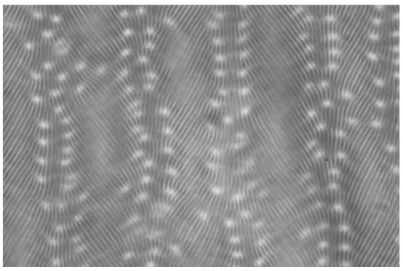

FIG. 6. Chevrons with double defect lines for a sample of thickness $d=42\ \mu$m.

under the microscope, the defects are generated and recombine only in pairs of opposite polarity. Furthermore, they have an anisotropic mobility. Namely, the defects move faster perpendicular to the rolls (''glide''), i.e., parallel to the mean direction of the director. With increasing voltage, the density of the defects becomes higher and the motion becomes faster, but there are no obvious spatial correlations. This is a typical state of defect chaos or defect turbulence. We have not attempted to study the onset of disorder since here the defect density becomes very low.

At a fairly well-defined value of $V_0=V_{chev}$ [or $\epsilon_{chev}=(V_{chev}^2-V_c^2)/V_c^2$] a reorganization is initialized rather suddenly. Defects of equal topological charge have a tendency to align themselves in chains along the y direction; see Fig. 5(c). This alignment leads to a superstructure that is (ideally) periodic in the x direction with period λ_{chev}. The topological charge of defects alternates from chain to chain. Together with this effect arises an alternating tilt of the original rolls, which can be characterized by a tilt angle δ with respect to the y axis. This effect constitutes the chevrons. Although the defect chains (essentially) do not move on average, there are fluctuations. Sometimes defects are generated or annihilated in the space between the chains. This is connected with a local separation of the chains larger or smaller than λ_{chev}, respectively. The modulation of chains along x can be seen in Fig. 5(c). λ_{chev} is about $4d$ and decreases slowly with increasing voltage; see Fig. 5(d).

At some higher voltage collective motion of defects along the chains becomes noticeable. Positively charged defects, e.g., those in the first fully visible chain to the left in Fig. 5(d), move in the negative y direction [downward in Fig. 5(d)], whereas the oppositely charged defects move in the opposite direction. With increasing V_0 the velocity increases, the chains become better aligned, and the rate of generation and recombination of defects decreases. Finally, thicker cells (d above about 38 μm) show at higher voltage the tendency to form double chains of equally charged defects. An example is shown in Fig. 6.

In the following we want to quantify some of the above observations. To investigate aspects of the statistics of the defects, we used a defect recognition algorithm based on the demodulation method developed in [22]. This method is based on the description of a two-dimensional modulated stripe pattern by $u(x,y)=A(x,y)e^{iq_m x}+\text{c.c.}+\text{higher}$ harmonics. The separation into the carrier wave with wave vector $(q_m,0)$ in the x direction and the complex amplitude function $A(x,y)$ is possible as long as A varies slowly on the scale $2\pi/q_m$. Note that A describes amplitude and phase modulations. We determine A as follows. First, we perform a

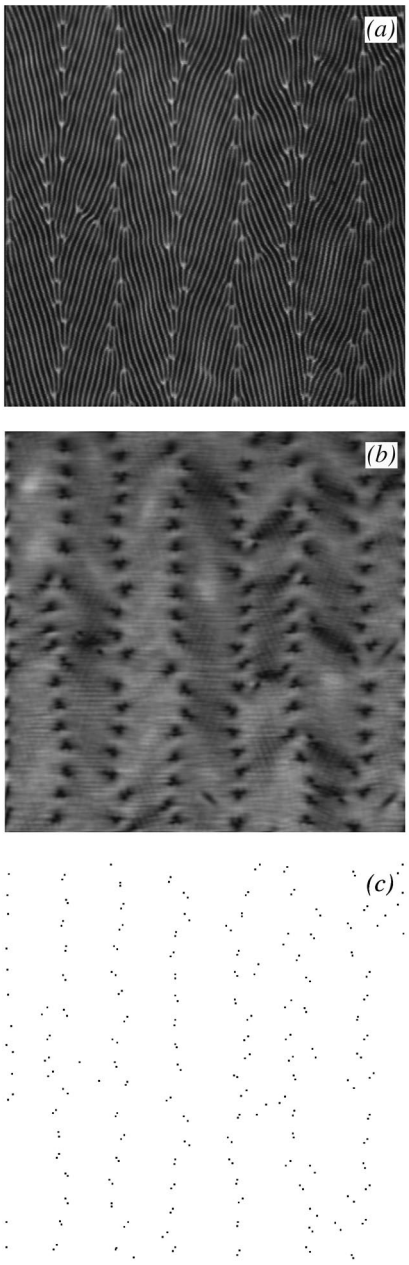

FIG. 7. Demodulation of a shadowgraph image. (a) Typical shadowgraph of a chevron pattern at $f=45$ Hz and $\epsilon=0{,}34$. (b) Square of the complex amplitude $A(x,y)$; the minima (zeros) are black. (c) Positions of the zeros of the complex amplitude in real space.

complex two-dimensional fast Fourier transform of $u(x,y)$. Second, a half plane in Fourier space (say, $q>0$) is selected. Third, the Fourier transform is set equal to zero in the other half plane and this function is transformed back to real space; thus $b(x,y)=A(x,y)e^{iq_m x}$ is obtained. For convenience we shift in addition the origin in Fourier space to $(q_m,0)$, where q_m is the first maximum of the Fourier transform on the real axis. In this way one is left with the slowly varying function $A(x,y)$, whose zeros give the locations of the defects. (Actually, the determination of q_m need not be very precise.) Figure 7(b) shows an example of $|A(x,y)|^2$ in a gray scale. Clearly $|A(x,y)|$ approaches zero (black) at the center of each defect. More precisely, we define the center of a defect

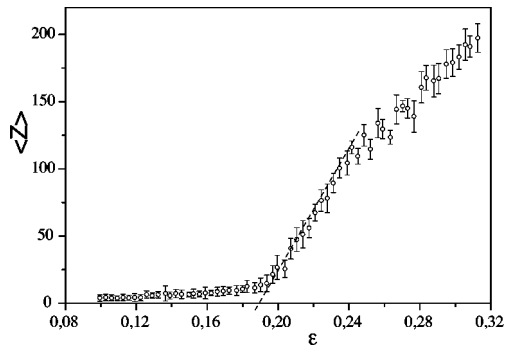

FIG. 8. Mean number $\langle Z \rangle$ of defects per image as a function of the control parameter ϵ for a sample thickness of 24 μm and an image size of 307×325 μm^2. $d=24$ μm and $f=45$ Hz.

as the location where the real and the imaginary parts of $A(x,y)$ become zero. As shown in Fig. 7(c), well-defined locations for the defects are obtained. (Due to the selected focal plane, each defect is characterized by the ending of two dark stripes, giving rise to two neighboring zeros.) As mentioned above, the topological charge of the defect can be determined by analyzing the behavior of the phase in the vicinity of the zero.

With the help of this defect recognition, we have determined the average number of defects in an image of size 307×235 μm^2. For each measurement 15 images were recorded with a time delay of 5 s. As shown in Fig. 8, the average numbers of defects increases with the control parameter ϵ. ($\epsilon=0$ still corresponds to the onset of dielectric rolls.) Three regimes can be distinguished. For $\epsilon<0.2$ the number of defects is small and increases slowly. At $\epsilon=0.2$ a fairly sharp transition to a rapid, roughly linear increase takes place. The slope decreases beyond $\epsilon=0.24$.

Next, spatial correlations of the defects are investigated by calculating distances Δx between all defects (irrespective of topological charge) in the x direction (parallel to the undistorted director). The resulting histogram $H(\Delta x)$ is shown in Fig. 9(a) for a well-developed chevron structure. Due to the finite size of the image, the number of defect pairs drops off linearly with increasing Δx. Consequently, the peaks in Fig. 9(a) decrease in amplitude as Δx increases. It is easily seen that the finite-width effects can be corrected by the distribution function $P(\Delta x)=H(\Delta x)/\langle Z\rangle(\Delta x_B+1-\Delta x)$, which is shown in Fig. 9(b). Note that this quantity is actually a correlation function. One clearly sees the long-range correlations of the periodic chevron structure. In order to fit the distribution, we found it easier to go over to the corresponding distribution function $P^*(\Delta x)$ for defects of one topological charge, which is shown in Fig. 10. It can be fitted by Gaussian distributions, as it is indicated by a broken curve in Fig. 10.

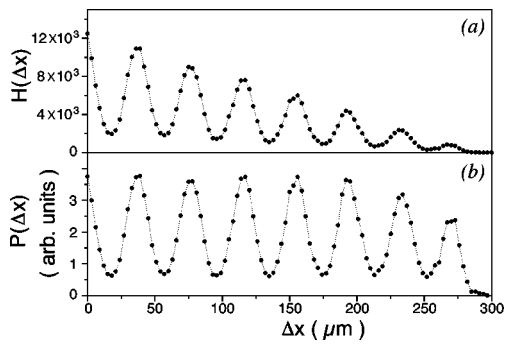

FIG. 9. Histogram of the distances in the x direction between defects. (a) Direct experimental result and (b) result with correction for the finite size effect. $d=24$ μm and $f=45$ Hz.

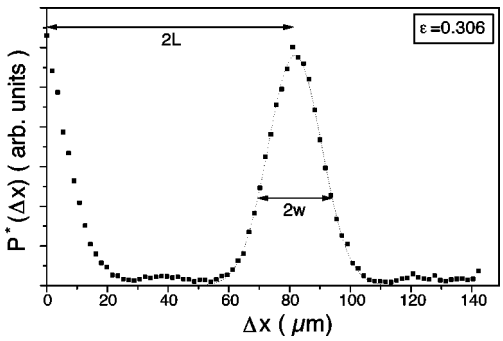

FIG. 10. Histogram of the distances in the x direction between defects of the same topological charge. The dotted curve represents a fit by a Gaussian distribution. $d=24$ μm and $f=45$ Hz.

Generally the distribution of defect distances in the x direction can be fitted reasonably well by a superposition of Gaussian distribution functions centered at the different chain positions:

$$P(\Delta x)=\frac{A}{\sqrt{2}w}\sum_j \exp\left(-\frac{(\Delta x-jL)^2}{2w^2}\right), \tag{3}$$

where w is the width, L the periodicity, and A a prefactor. In Fig. 11 histograms are shown together with the fits for different values of ϵ. Actually, the fit is used merely to extract from the measurements an order parameter A_{chev} character-

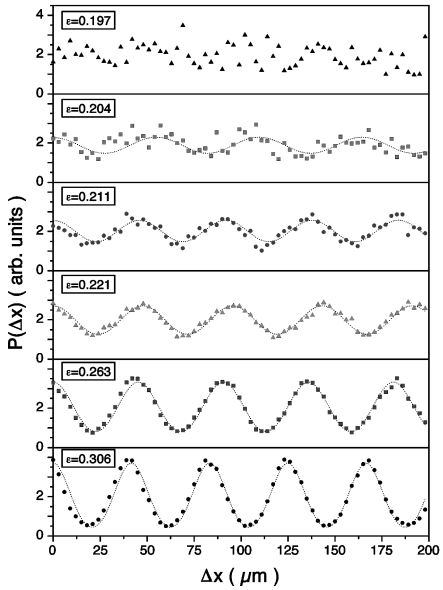

FIG. 11. Histograms of the distances in the x direction between defects for different values of ϵ. The dotted curves represent fits by a superposition of Gaussian distributions according to Eq. (3). $d=24$ μm and $f=45$ Hz.

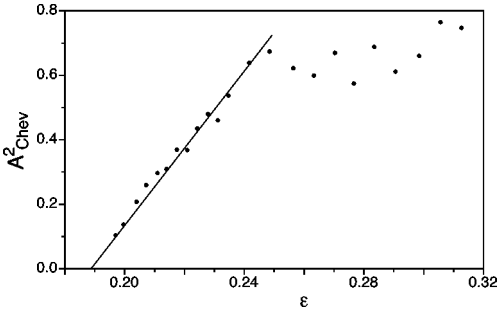

FIG. 12. Chevron amplitude A^2_{chev} as extracted from histograms (Fig. 11) versus control parameter ϵ. Results are shown only where the fitting with Eq. (3) was successful. The solid line represents a linear fit. $d=24$ μm and $f=45$ Hz.

izing the chevron state. We choose the following direct measure of the chevron amplitude:

$$A^2_{chev}=\frac{P_{max}(\Delta x)-P_{min}(\Delta x)}{P_{max}(\Delta x)+P_{min}(\Delta x)}=\sum_{n=1}^{\infty}\exp\left(-\frac{\pi}{2}\frac{w^2}{L^2}n^2\right). \tag{4}$$

Since $P(\Delta x)$ is insensitive to the topological charge, the quantity A^2_{chev} indeed has to be associated with the square of the order parameter. The last expression in Eq. (4) can be obtained by Fourier expansion of $P(\Delta x)$. It shows that A_{chev} is determined by the ratio w/L alone. It is easy to see that for small values of A_{chev} our fitting procedure becomes equivalent to a harmonic fit. In Fig. 12, A^2_{chev} is plotted versus ϵ. The initial rise of A^2_{chev} is found to be roughly proportional to $\epsilon-0.19$, i.e., the formation of chevrons appears to follow a forward bifurcation. The bifurcation point $\epsilon=0.19$ coincides with the onset of the pronounced increase of the defect density in Fig. 8. We point out that a determination of the onset of spatial correlations by naive inspection of the (disordered) patterns leads to large uncertainties; see, e.g., Fig. 13.

Figure 13 also illustrates that the rotation of the rolls away from the normal direction (perpendicular to the undistorted director) is connected with the presence of defects. A simple geometric construction shows that in sufficiently well-developed chevrons, where most defects are confined to the chains, the angle δ away from the normal orientation satisfies the (topological) condition

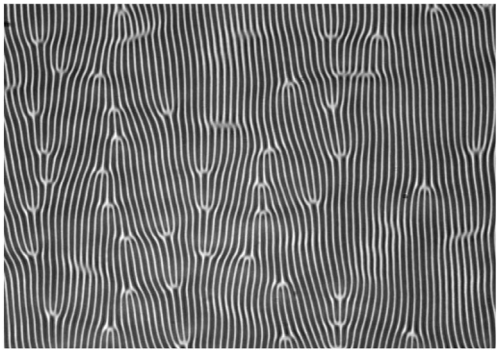

FIG. 13. Snapshot of the defect pattern for $\epsilon=0.207$ slightly above the chevron threshold.

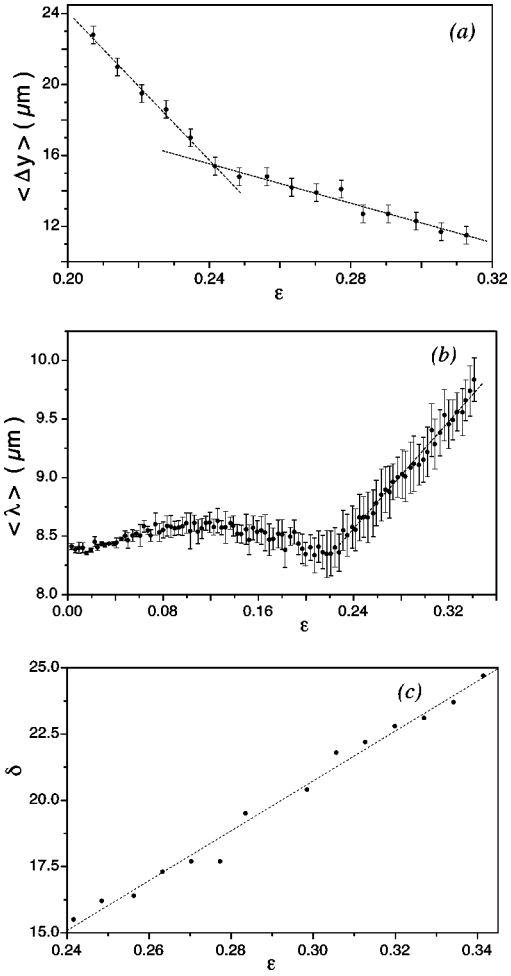

FIG. 14. (a) Mean distance between defects in the direction of the chain, (b) mean wavelength $\langle\lambda\rangle$ of the dielectric rolls in x direction, and (c) tilt angle of the rolls versus the control parameter ϵ. $d=24$ μm and $f=45$ Hz.

$$\tan(\delta)=\frac{\lambda}{2\Delta y}. \tag{5}$$

Here λ and Δy designate the wavelength of the roll pattern in the x direction and the mean separation of defects along the chain, respectively. In Fig. 14 we show how these quantities develop as a function of the control parameter ϵ. λ was determined from the Fourier transform of x-line scans from shadowgraph images. It exhibits a pronounced change in its ϵ dependence in the vicinity of the chevron threshold. Δy initially decreases rather steeply. At $\epsilon=0.24$ the decrease becomes slower, which we interpret as the crossover to fully developed chevrons. The tilt angle δ is well defined above this transition point and exhibits a linear increase for $\epsilon>0.24$ as shown in Fig. 14(c).

In summary, we have demonstrated that chevrons arise in a fairly sharp transition that is characterized rather easily by the sudden increase of the mean number of defects or by the onset of spatial correlations. Thus we can define a secondary

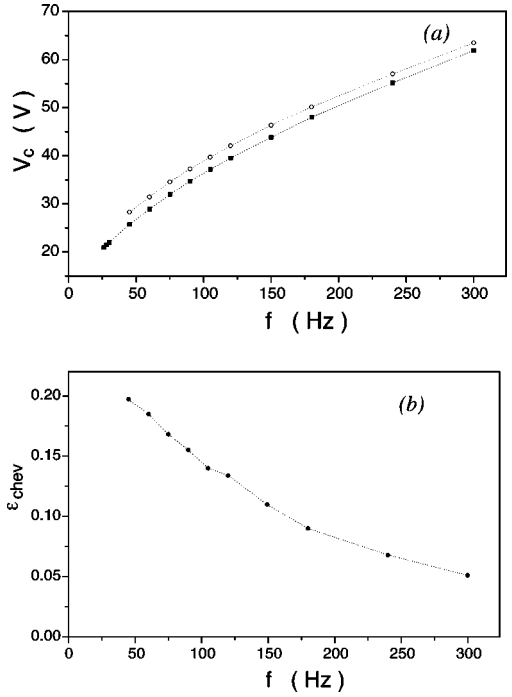

FIG. 15. (a) Critical voltage for the appearance of dielectric rolls (solid circles) and for the occurrence of chevrons (open circles) and (b) critical control parameter ϵ_{chev} versus frequency.

threshold $V_{chev}(f)$ and an $\epsilon_{chev}(f)$, respectively, in the voltage-frequency plane, which is shown in Fig. 15. The difference between the secondary and the primary threshold decreases from 2.5 V($\epsilon_{chev}=0.18$) at $f=50$ Hz to 1.3 V ($\epsilon_{chev}=0.05$) at 300 Hz. A similar decrease was observed previously in experiments on the material MBBA [2]. Its significance will be discussed in the next section.

V. CONCLUSION AND DISCUSSION

We hope that the quantitative results presented here will stimulate theoretical work. Recently a theory of chevrons was proposed [13]. Although it cannot, as it stands, be used directly for quantitative comparison with our experiments, some scaling properties can be adopted. The theory starts from a homogeneous planar director field **c** (actually a two-dimensional unit vector) that is weakly oriented by an external torque. Such a situation is found in particular in homeotropically oriented samples after a primary bend Freédericksz transition, which tilts the director **n** away from the homeotropic orientation. The resulting planar component represents **c**, which is (ideally) not fixed externally, unless a (weak) stabilizing magnetic field is applied. After the system has gone through the transition to electroconvection a description near threshold is provided by two coupled equations that describe the dynamics of the patterning mode and **c** [23]. Simulations show that these equations can produce chevrons via a scenario that is consistent with the one described here.

The key to the formation of chevrons is an ''anomalous torque,'' which destabilizes the normal orientation of the **c** director perpendicular to the rolls. The hydrodynamic description of nematic liquid crystals gives quite generally such a torque. Its strength grows with ϵ [23,24] and will quickly overcome the external torque. This destabilizes eventually the pattern and leads to defect chaos, as observed. The formation of chevrons at larger ϵ can be captured by a further reduced (coarse-grained) description in terms of reaction-diffusion equations, which governs the topological charge density ρ and the in-plane director angle ϕ. (ϕ is defined as the angle between **c** and the normal to the roll direction.) Due to the anomalous torque, ϕ plays the role of an activator that can spontaneously grow. This activates a (local) topological charge imbalance, since the rolls tend to follow the rotation of the director (this paradoxical behavior cannot occur in a potential system). The reorientation of rolls entails the motion of defects with oppositely charged defects moving in opposite direction. Postulating a diffusion length for the inhibitor ρ that is shorter than the correlation length of the activator, a situation arises that can destabilize towards a stationary periodic pattern (diffusive or Turing instability). The resulting supercritical bifurcation explains the formation of chevrons and ϵ_{chev} scales with the square of the magnetic field. The damping of ρ must overcome the activation of ϕ since otherwise there is a Hopf bifurcation towards a homogeneous oscillating state.

Electroconvection in the dielectric regime of planarly aligned cells shares important features with the homeotropic system. Due to the fact that the wavelength $2\pi/q$ of the rolls is small compared to the cell thickness, the in-plane director mode, which is now connected with a twist deformation, is also here a soft degree of freedom. Although the weakly nonlinear descriptions are somewhat different in the two systems [21], one expects also here chevrons to be produced by the same mechanism. This demonstrates one of the most interesting aspects brought out by the theory, namely, that chevrons are a universal feature to be expected in a class of systems with a soft planar director mode. One expects that the quantity $1/qd$ plays the role of the magnetic field in the homeotropic case so that here ϵ_{chev} should decrease with increasing frequency ($q\sim f^{1/2}$), as observed. (Incidentally, chevrons have been observed in homeotropic convection [25].)

The optical method used in this investigation is the usual one that is sensitive only to the out-of-plane component of the director. As a consequence, the important twist mode of the director could not be detected. In a very recent work the structure of chevrons was studied by a sophisticated method, which allows us to detect and to measure (semiquantitatively) the twist deformation [26]. The results indicate that in the interchain regions the director is indeed twisted strongly in accordance with the model.

Further studies of the statistical properties of the defect chaotic state (production rate and lifetime of defects, etc.) appear desirable and are under way. A connection between the appearance of spatial ordering of the defects and the increase of the defect density should be established. It appears likely that the sudden increase of the defect density is only a consequence of the ordering, which reduces the probability that defects of opposite polarity come near each other. This should result in an increase of the lifetime without an (appreciable) increase of the production rate. Also, the properties of the well-developed chevron state are under study. Namely, the drift of defects, which appears to go together

with a mean flow in the velocity field, and the appearance of the disclination loops in the director field that eventually initiate the evolution towards a strongly turbulent state are under study. Presumably these disclinations are a result of reconnection processes of the director field that occur in the central portion of the layer as a consequence of the strong in-plane director deformations.

ACKNOWLEDGMENTS

We wish to thank C. Haite, W. Pesch, A. G. Rossberg, and P. Toth for useful discussions and help with the image analysis. Financial support by the Deutsche Forschungsgemeinschaft (Grant No. DFG-Kr690/12) and the TMR program ''Patterns, Noise and Chaos'' of the EU is gratefully acknowledged.

[1] I. Rehberg, B. L. Winkler, M. de la Torre Juarez, S. Rasenat, and W. Schöpf, Adv. Solid State Phys. **29**, 35 (1989).
[2] S. Kai and W. Zimmermann, Prog. Theor. Phys. Suppl. **99**, 458 (1989).
[3] L. Kramer and W. Pesch, in *Pattern Formation in Liquid Crystals*, edited by A. Buka and L. Kramer (Springer-Verlag, New York, 1995), Chap. 6, and references therein.
[4] W. Helfrich, J. Chem. Phys. **51**, 4092 (1969).
[5] Orsay Liquid Crystal Group, Phys. Rev. Lett. **26**, 1642 (1970); E. E. Dubois-Violette, P. G. de Gennes, and O. J. Parodi, J. Phys. (Paris) **32**, 305 (1971).
[6] I. Smith, Y. Galerne, S. Lagerwall, E. Dubois-Violette, and G. Durand, J. Phys. Colloq. **36**, C1-237 (1975).
[7] F. H. Busse, in *Hydrodynamic Instabilities and the Transition to Turbulence*, edited by H. L. Swinney and J. P. Gollub (Springer-Verlag, Berlin, 1986).
[8] M. C. Cross and P. C. Hohenberg, Rev. Mod. Phys. **65**, 851 (1993).
[9] U. Schneider, M. de la Torre Juárez, and W. Zimmermann, Phys. Rev. A **46**, 1009 (1992).
[10] R. Stannarius, M. Grigutsch, and H. Amm (unpublished).
[11] W. Kriegbaum and H. Lader, Mol. Cryst. Liq. Cryst. **62**, 87 (1980).
[12] S. Chandrasekhar, *Liquid Crystals* (Cambridge University Press, Cambridge, 1992); P. G. de Gennes and J. Prost, *The Physics of Liquid Crystals* (Clarendon, Oxford, 1993); L. M. Blinov, *Electrooptical and Magnetooptical Properties of Liquid Crystals* (Wiley, New York, 1983).
[13] A. G. Rossberg and L. Kramer, Physica D **115**, 19 (1998).
[14] S. Rasenat, G. Hartung, B. L. Winkler, and I. Rehberg, Exp. Fluids **7**, 412 (1989).
[15] E. Bodenschatz, W. Zimmermann, and L. Kramer, J. Phys. (Paris) **49**, 1875 (1988).
[16] W. Decker, Doctoral thesis, Bayreuth, 1995 (unpublished); A. Hertrich, Doctoral thesis, Bayreuth, 1995 (unpublished).
[17] In *Pattern Formation in Liquid Crystals* (Ref. [3]), p. 234, the voltage must be taken as the peak-to-peak voltage.
[18] M. Treiber, N. Eber, A. Buka, and L. Kramer, J. Phys. II **7**, 649 (1997).
[19] $d=24.0\ \mu$m, $k_{33}=13.5\times10^{-12}$ N, $\sigma_{\parallel}=0.48\times10^{-8}$ 1/(Ωm), $\sigma_{\parallel}/\sigma_{\perp}=1.66$, and $f_c/f_d=1.59$.
[20] Only in a small region of the conduction regime where one has oblique rolls are some indications that the bifurcation is slightly subcritical.
[21] Preliminary results can be found in A. Lindner, Diploma thesis, Bayreuth, 1997 (unpublished).
[22] S. Rasenat, Doctoral thesis, Bayreuth, 1991 (unpublished).
[23] A. G. Rossberg, A. Hertrich, L. Kramer, and W. Pesch, Phys. Rev. Lett. **76**, 4729 (1996).
[24] E. Plaut, W. Decker, A. Rossberg, L. Kramer, and W. Pesch, Phys. Rev. Lett. **79**, 2367 (1997).
[25] P. Toth, A. Buka, J. Peinke, and L. Kramer, Phys. Rev. E (to be published).
[26] H. Stannarius, H. Amm, and A. G. Rossberg (unpublished).